J Mater Sci (2013) 48:1555–1561
DOI 10.1007/s10853-012-6911-3

Synthesis and characterization of single crystalline $GdB_{44}Si_2$ nanostructures

Jinshi Yuan · Han Zhang · Jie Tang · Norio Shinya · Yuexian Lin · Lu-Chang Qin

Received: 23 July 2012 / Accepted: 19 September 2012 / Published online: 6 October 2012

Abstract $GdB_{44}Si_2$ is an excellent thermoelectric material, and nanostructured $GdB_{44}Si_2$ makes it possible to potentially improve its properties further. $GdB_{44}Si_2$ nanowires and nanobelts have been fabricated by chemical vapor deposition and characterized by electron diffraction and high-resolution electron microscopy. These nanostructures are of the YB_{50} structure and grew in the [010] direction. The nanowires have thickness of less than 100 nm and length of several tens of microns. The nanobelts have thickness of about a few tens of nanometers. Morphological and compositional analyses confirmed that the nanowire growth followed the vapor–liquid–solid mechanism and the nanobelts were formed by a subsequent vapor–solid process of condensation.

Introduction

Boron (B) is the lightest non-metallic element in the solid form and has numerous attractive properties, including a low mass density, high melting point, high hardness, and high Young's modulus [1, 2]. As a result, it is often used in high temperature and/or light weight applications as coatings or in other forms [3]. During the last 20 years, many rare-earth B-rich compounds have been synthesized for their interesting structures and possible applications [4]. In the rare-earth B-rich compounds, the boron atoms form an electron-deficient network and the rare-earth atoms are lying in the voids of the framework to afford extra electrons to stabilize the whole structure. This combination leads the rare-earth B-rich compounds to possess interesting magnetic and electric properties [4]. Among the rare-earth B-rich compounds, the $RB_{44}Si_2$ compounds (R stands for rare earth element) were found to have high melting points (about 2300 K), large Seebeck coefficients (greater than 200 μV/K at temperatures above 1000 K), and thermal conductivity as low as 1.5 W/m/K [5, 6]. Therefore, they are promising candidates for thermoelectric applications.

$RB_{44}Si_2$ are of the RB_{50} structure which was first obtained in YB_{50} by Tanaka et al. [7]. RB_{50} also forms for the rare earth elements of Tb, Dy, Ho, Er, Tm, Yb, and Lu [8]. Because of the large atomic radius of Gd, GdB_{50} was considered impossible and has not been obtained so far. On the other hand, by adding a small amount of Si into the synthesis system, yttrium borosilicide, $YB_{41}Si_{1.0}$, was made by Tanaka et al. [9]. They also found that the doping of Si enlarged the lattice constants and made it possible to obtain a Gd B-rich compound of the RB_{50} structure [10, 11]. By now, there have been several different rare-earth borosilicides reported in the literature including $YB_{41}Si_{1.2}$ [12], $TbB_{44}Si_{0.7}$ [13], and $YbB_{45.6}Si_{1.0}$ [14]. The major difference between these rare-earth B-rich compounds is the occupancy of B and Si in the structures [12]. Since the structural differences do not impact much the properties of rare earth borosilicides, here we use $RB_{44}Si_2$ to represent these rare earth borosilicides as Mori et al. suggested [8].

J. Yuan · J. Tang (✉) · N. Shinya · Y. Lin
National Institute for Materials Science, Sengen, Tsukuba 305-0047, Japan
e-mail: tang.jie@nims.go.jp

J. Yuan · J. Tang · Y. Lin
Graduate School of Pure and Applied Sciences, University of Tsukuba, Tsukuba 305-8577, Japan

H. Zhang
International Center for Young Scientist, National Institute for Materials Science, Sengen, Tsukuba 305-0047, Japan

L.-C. Qin (✉)
Department of Physics and Astronomy, Curriculum in Applied Sciences and Engineering, University of North Carolina at Chapel Hill, Chapel Hill, NC 27599-3255, USA
e-mail: lcqin@email.unc.edu

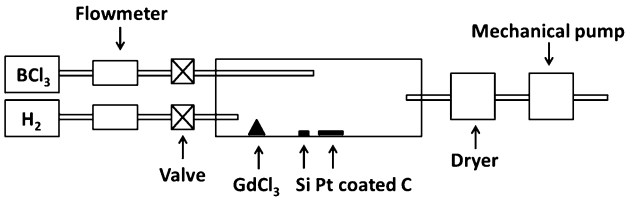

Fig. 1 Schematic of CVD system for synthesis of rare-earth B-rich nanostructures. In this work, the graphite (C) substrate was placed at the center of the tube furnace and $GdCl_3$ was placed some distance away. The reaction tube was first evacuated to 10^{-1} Pa by a mechanical pump before it was heated to target temperature. Vaporized $GdCl_3$ was carried by H_2 gas to the surface of the substrate. When the temperature at the center of the tube reached 1200 °C, BCl_3 was introduced by a separate quartz tube over to the substrate and mixed with $GdCl_3$ vapors to produce the B-rich nanostructures. The substrate was coated with Pt as catalyst and Si was placed beside the substrate to afford Si for catalysis and formation of the nanostructures

In this work, we report the first synthesis of $GdB_{44}Si_2$ nanowires and nanobelts by chemical vapor deposition (CVD) and structural characterization by scanning electron microscopy, electron diffraction, transmission electron microscopy, and energy-dispersive X-ray spectroscopy. The growth mechanisms of the nanowires and nanobelts are also examined, described, and discussed in terms of the vapor–liquid–solid (VLS) and vapor–solid (VS) growth models.

Experimental

In our experiment, gadolinium trichloride ($GdCl_3$) and boron trichloride (BCl_3) were used as reactant precursors to supply Gd and B in the reactions. The synthesis system and process are similar to those used in our work for synthesizing rare-earth hexaboride (RB_6) nanostructures [15–17] based on the following chemical reaction

$$2\ GdCl_3(g) + 88\ BCl_3(g) + 135\ H_2(g) + 4\ Si = 2\ GdB_{44}Si_2(s) + 270\ HCl\ (g). \quad (1)$$

The main difference is the ratio of $GdCl_3$ gas and BCl_3 which is much lower for the synthesis of higher borides than for RB_6. The reaction was conducted in a quartz tube furnace. A schematic of our system is shown in Fig. 1. $GdCl_3$ powders (Sigma Aldrich, 99.95 % purity) were put in the relatively low temperature zone of the tube furnace. A graphite plate (1 cm × 2 cm) was placed at the center of the quartz tube as substrate. We used an alloy of platinum (Pt) and silicon (Si) as catalyst. A Pt thin film of 20 nm in

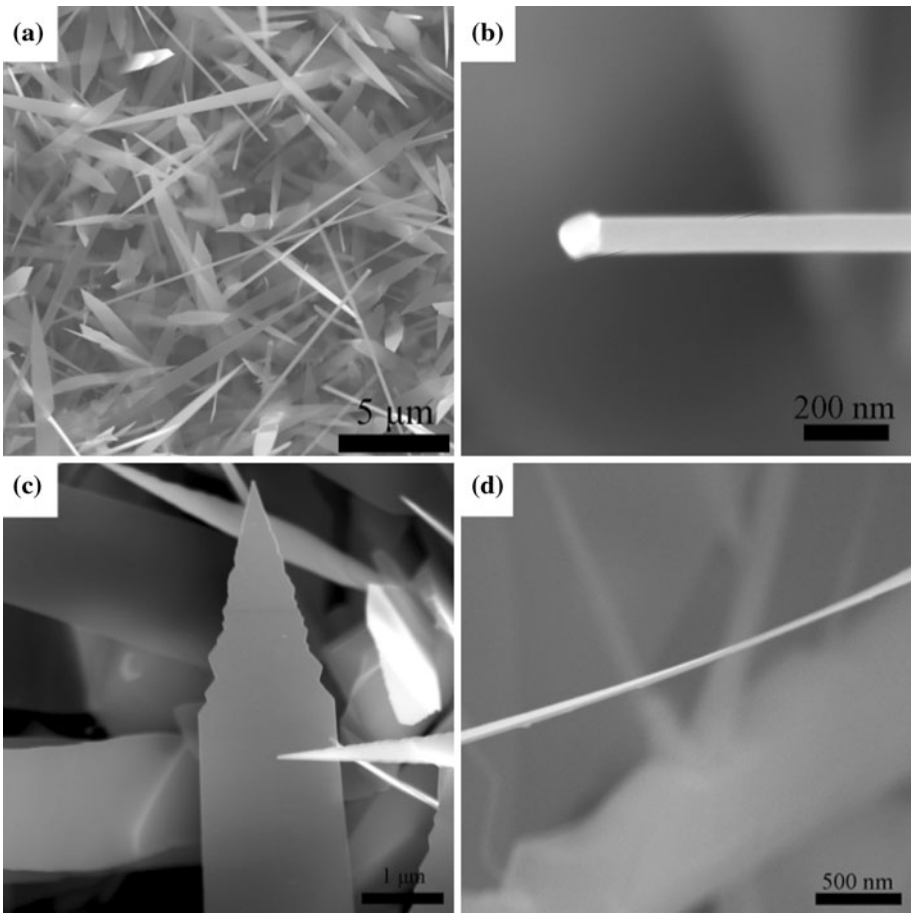

Fig. 2 **a** SEM image of the surface of substrate with nanowires and nanobelts grown and mixed together. **b** A single nanowire with a catalyst particle at its tip. **c** *Top view* of a typical nanobelt. **d** *Side view* of a nanobelt to reveal its uniform thickness

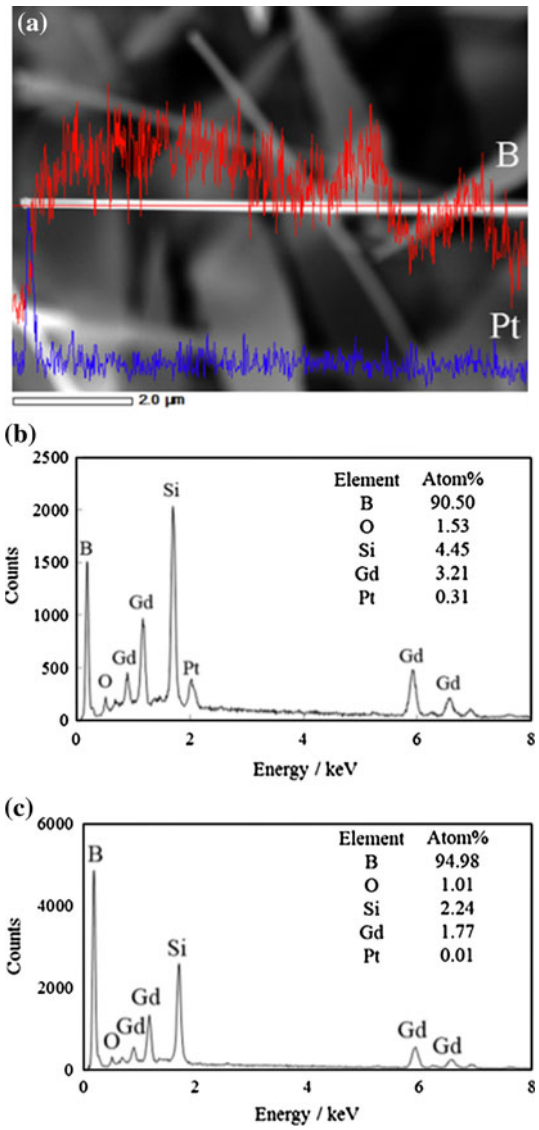

Fig. 3 **a** Line-scan of EDS data along a single nanowire. Only *B* and *Pt* were observed and their respective line-scan spectra are displayed in *red* and *blue*, respectively. **b** EDS result collected from the catalyst particle. **c** EDS result collected from the nanowire body (Color figure online)

thickness was coated on the substrate by sputtering and a piece of Si flake was placed just beside the graphite substrate. The tube furnace was evacuated to below 10^{-1} Pa and heated. The $GdCl_3$ vapors were carried over to the substrate by a flow of hydrogen (H_2) gas. When the central part of the quartz tube was heated to 1200 °C, BCl_3 gas was allowed into the reaction zone through a quartz tube. After 5 min of reactions, heating was stopped and the synthesis process was terminated. The substrate with boron nanostructures was subsequently examined using field emission scanning electron microscopy (FE-SEM, JSM-7001F) equipped with energy-dispersive X-ray spectrometer (EDS) and transmission electron microscopy (TEM, JEM-2100F) for structural characterization.

Results and discussion

Morphology of $GdB_{44}Si_2$ nanostructures

Figure 2 shows the SEM images of the nanostructures obtained on the substrate. In Fig. 2a, both nanowires and nanobelts are observed clearly. The nanowires have lengths of several tens of microns and thickness of less than 100 nm. In some other areas not shown in this figure, we could even find nanowires as thin as 15 nm. Figure 2b is the morphology of a single nanowire which is straight and has a smooth surface. As a typical structural feature, at the end of the nanowire, a catalyst particle is usually observed, indicating that the mechanism responsible for the formation and growth of the nanowires is the vapor–liquid–solid (VLS) mechanism, which was initially established by Wagner [18] to account for growth of whiskers. In the VLS growth mechanism, during the growth process of whiskers, catalyst droplets were formed first and these droplets adsorbed product atoms present in the gaseous phase. After supersaturation of product atoms in a catalyst droplet is reached, the product atoms would condense and deposit on the interface between the droplet and the substrate continuously to result in the formation and growth of a nanowire. Therefore, a nanowire tip with a catalyst particle is usually taken as the evidence of this mechanism in action. Figure 2c, d show the top and side views of typical nanobelts. The width of the nanobelt in Fig. 2c is about 2 μm and the thickness of the nanobelt in Fig. 2d is about 15 nm. As shown in Fig. 2a, c most of the nanobelts are of similar morphology consisting of a bottom part with a uniform width and a contracted tip.

$GdB_{44}Si_2$ nanowires

Figure 3a is a line-scan of energy-dispersive X-ray spectrum (EDS) acquired along a nanowire. Since the signals of other elements, including Gd, Si, and O, are very low, here we only listed B and Pt for comparison, plotted in red and blue, respectively. From the EDS data, it is clear that the major element of the nanowire is B while Pt only exists in the catalyst particle at the tip of the nanowire which agrees well with Fig. 3b. Figure 3b, c show the EDS results collected from the catalyst particle and the nanowire body, respectively. Elements of B, O, Gd, and Si were observed in both spectra. The existence of O means that the nanowires were partly oxidized, which occurred either during synthesis or in the air after synthesis since the sample was not stored in vacuum or inert atmosphere. Comparing Fig. 3b, c the concentrations of Si and Gd are much higher in the catalyst than in the nanowire body. Taking the fact into consideration that the melting temperature of Pt, which is 1768 °C, is much higher than the temperature that we

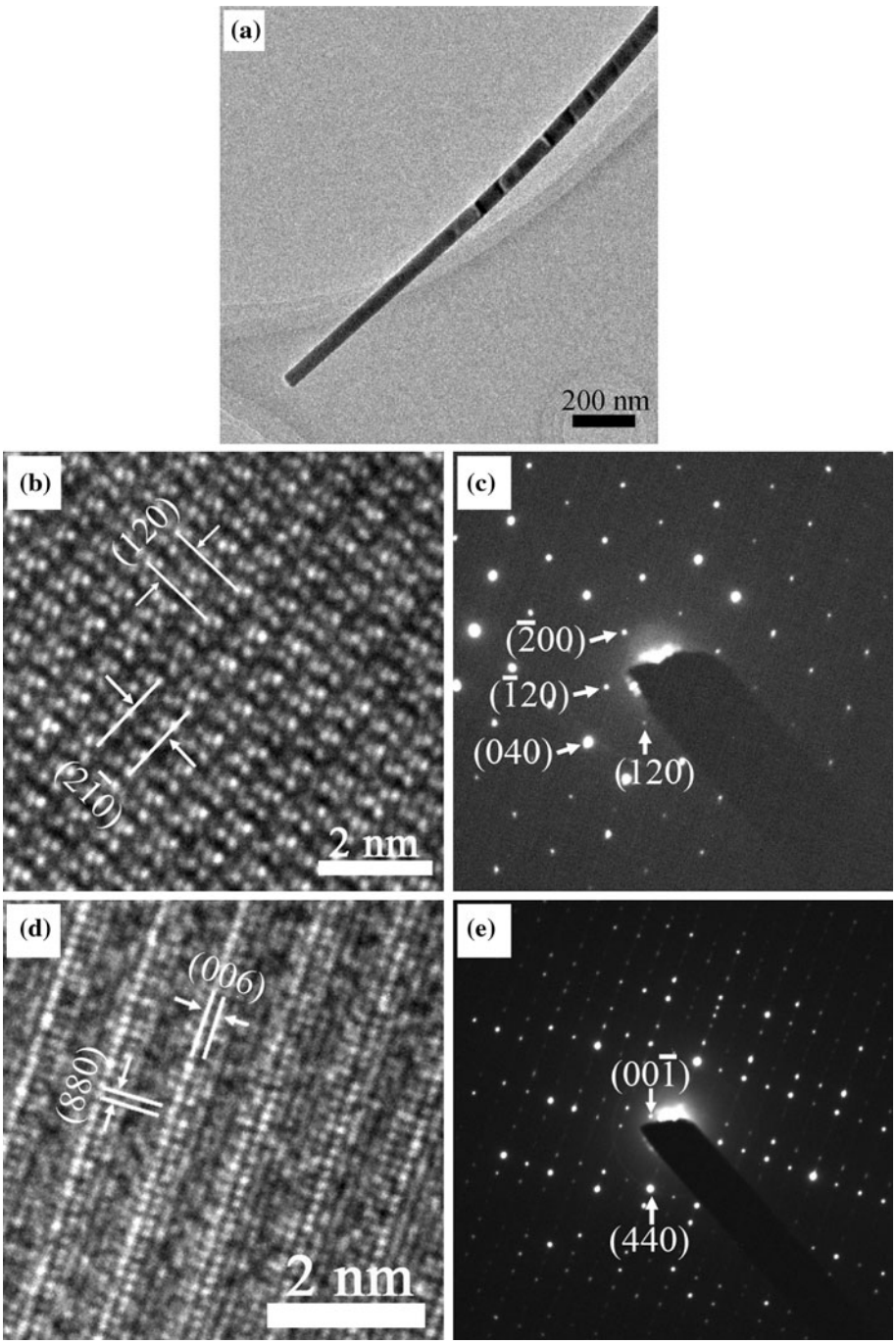

Fig. 4 **a** Low-magnification TEM image of a single nanowire. **b**, **c** HRTEM image and SAED pattern of the nanowire shown are taken in the [001] direction. The spacings of the (120) and $(2\bar{1}0)$ *planes* are shown in **b**. **d**, **e** HRTEM image and SAED pattern of the nanowire shown are taken in $[1\bar{1}0]$ direction. The lattice spacings of the (006) and (880) *planes* are indicated in **d**

applied in the synthesis, we believe that the catalyst is a Pt–Si alloy or even Pt–Si–Gd alloy which has a melting temperature lower than 1200 °C at which the nanostructures were synthesized.

Figure 4 shows the results of structural analysis of a typical single $GdB_{44}Si_2$ nanowire using electron diffraction and high-resolution electron microscopy (HRTEM). Figure 4a is a low-magnification TEM image showing that the nanowire has a thickness of about 40 nm. Figure 4b, c are an HRTEM image and a selected-area electron diffraction (SAED) pattern of the nanowire taken in the [001] direction, respectively. These images show clearly that the nanowire is single crystalline. The crystal structure of sintered polycrystalline $GdB_{44}Si_2$ has been well described by Mori [4], which has an orthorhombic lattice with lattice constants $a = 16.746$ Å, $b = 17.731$ Å, and $c = 9.565$ Å and space group *Pbam*. Figure 4b is an HRTEM image of the nanowire acquired in the [001] orientation, where the lattice planes

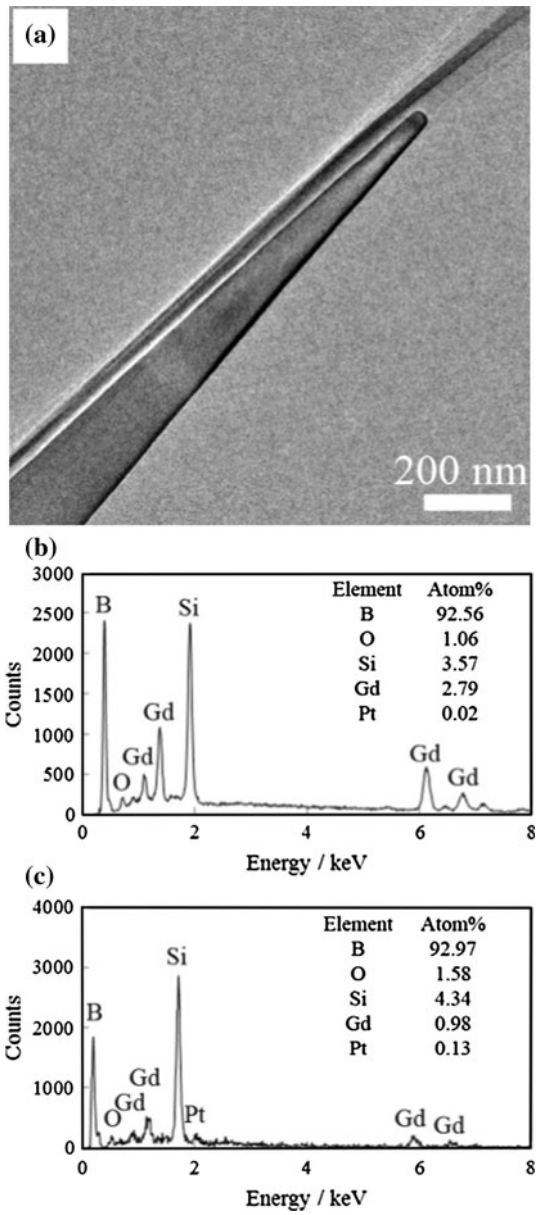

Fig. 5 **a** Low-magnification TEM image of a nanobelt. **b** EDS acquired from body of the nanobelt. **c** EDS collected from the tip of the nanobelt where the catalyst sits

(120) and $(2\bar{1}0)$ of spacings 7.84 and 7.57 Å, respectively, are indicated. From the corresponding electron diffraction pattern given in Fig. 4c, in which the Bragg reflections of $GdB_{44}Si_2$ with indices $(\bar{2}00)$, $(\bar{1}20)$, (040), and (120) are also indexed and indicated. It is determined that the nanowire grew in the [010] direction. Figure 4d, e are the HRTEM image and SAED pattern taken in the $[1\bar{1}0]$ direction from which we can observe two orthorhombic lattice planes with spacings of 1.59 and 1.52 Å, corresponding to the (006) and (880) lattice planes, respectively. In the electron diffraction pattern given in Fig. 4e, the reflections are also indexed to confirm that the nanowire is of the same structure.

$GdB_{44}Si_2$ nanobelts

High-resolution electron microscopy as well as electron diffraction has also been applied to characterize the structure of the nanobelts. Figure 5a is a low-magnification TEM image of the contracted tip of a nanobelt, which was selected for a detailed analysis. Figure 5b, c are the EDS results collected from the body and the tip of the nanobelt, respectively. From the EDS data we can observe that the difference in the chemical composition of the nanobelt is similar to that in the nanowire described earlier. There is also a Pt–Si alloy particle on the tip acting as catalyst and no Pt was detected in the body of the nanobelt. The concentration of Pt in the catalyst particle was lower than that in the nanowire. It is attributed to the fact that the catalyst particle is so small relative to the nanobelt and much more signals from the body of the nanobelt and even other nanostructures were actually collected.

Figure 6 are the HRTEM images and corresponding SAED patterns obtained from the nanobelt shown in Fig. 5a in two different crystallographic orientations, [001] and $[\bar{1}02]$. These images confirmed that the nanobelts are single crystalline and also of the same $GdB_{44}Si_2$ structure. Figure 6a reveals the inter-planar spacing of two orthogonal planes, as indicated in the figure, of spacings 16.75 and 17.73 Å, respectively, corresponding to the (100) and (010) lattice planes. The corresponding electron diffraction pattern is given in Fig. 6b. As indicated in the electron diffraction pattern where the Miller indices are also given, the (h00) and (0k0) reflections with h and k being odd are forbidden in this orientation because of the space group of *Pbam*. We also tilted the same nanobelt to other orientations in our TEM examinations. Figure 6c, d are the HRTEM image and corresponding SAED pattern taken in the crystallographic direction of $[\bar{1}02]$. The lattice planes of Miller indices (010) and (201) and their corresponding Bragg reflections of indices [010]* and [201]* are also indicated in the figures.

In addition, the EDS results helped to identify that the growth of the nanobelt also followed the VLS process. The most prominent characteristic of the growth of nanobelt in comparison with nanowire is that it has a secondary direction of growth besides the rapid growth in the axial direction [19–21]. Unlike the growth in the axial direction, there are no catalyst droplets on the side surfaces to make them preferential sites. Therefore, the vapor–solid (VS) growth mechanism is attributed to the morphology of the belt-like nanostructures which means that the produced atoms/molecules nucleate from the vapor and deposit on the substrate or the surface of the previously formed crystals [22]. A diffusion process is usually promoted to make the molecules to

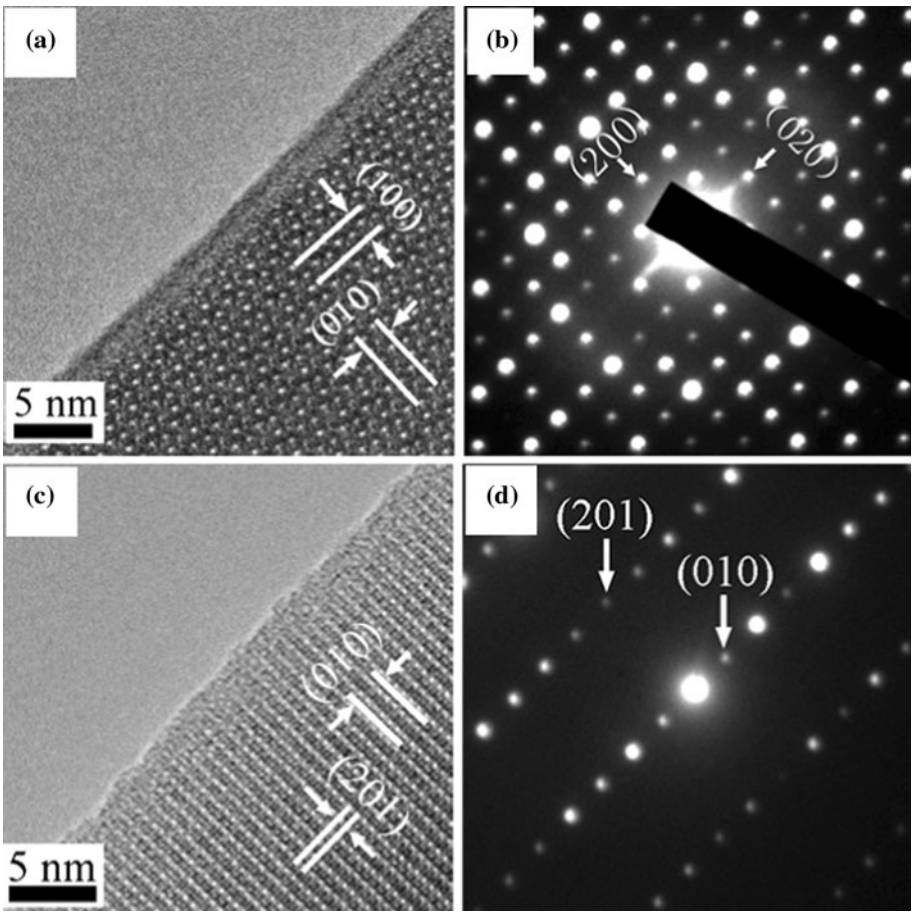

Fig. 6 **a**, **b** HRTEM image and SAED pattern of the nanobelt shown in Fig. 5a are taken in the [001] direction. The lattice *planes* of Miller indices (010) and (100) are indicated in the HREM image shown in **a** and their respective Bragg reflections are indicated in **b**. **c**, **d** HRTEM image and SAED pattern of the same nanobelt shown in Fig. 5a taken in the [$\bar{1}$02] direction. The presence of the otherwise extinction (010) reflection is due to double diffraction effect. The (201) and (010) lattice planes are indicated in the HREM image shown in **c**

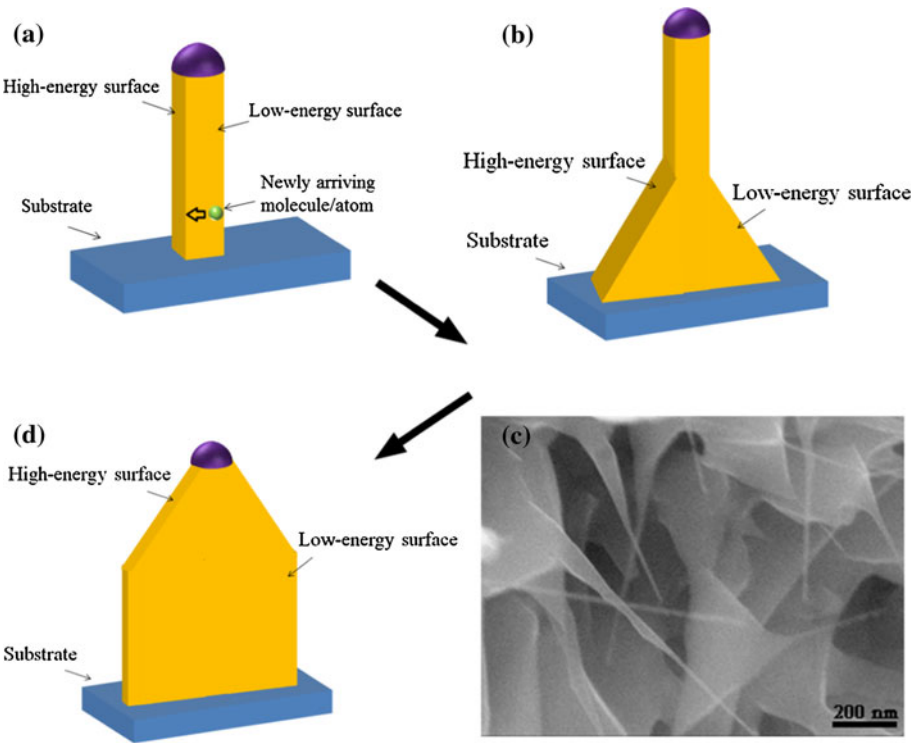

Fig. 7 Schematic illustration of the process of formation and growth of nanobelt involving both VLS and VS processes. **a** A growing nanowire with a catalyst droplet at the tip. The surfaces have different surface energy due to the structural and geometric constraints. The product has a higher probability to nucleate on low-energy surface and diffuse to and stick onto a surface of higher energy. **b** As the process is on-going, the low-energy surface enlarged and grew in two-dimensions. **c** SEM image of nanostructures whose growth was terminated during transition from nanowire to nanobelt. **d** Nanobelt was formed. The growth of the nanobelt along the lateral direction stops when the width reaches limit. The growth at the *bottom part* stops first to result in the morphology shown in this figure

stick onto the "rough" sites to lower the surface energy and/or for some other kinetic considerations [21]. In our process, the $GdB_{44}Si_2$ nanowires grew first on the substrate following the VLS mechanism, and then, since the supersaturation was high enough to stimulate the VS growth, extra molecules/atoms deposited on the side surfaces with different surface energy as illustrated in Fig. 7a. The choice of the side surface to which these molecules/atoms attach is strongly influenced by the need for surface energy minimization and kinetics during crystal growth [23]. The nucleation probability on the surface of a whisker was established to be

$$P_N = B\exp\left(-\frac{\pi\sigma^2}{k^2T^2\ln\alpha}\right), \quad (2)$$

where P_N is the nucleation probability, B a constant, σ the surface energy of the solid whisker, k the Boltzmann constant, T absolute temperature, and α the supersaturation ratio. Equation (2) indicates that the nucleation probability is higher on the surface with lower surface energy. On the other hand, since the molecules/atoms have lower binding energy on low-energy surfaces, it would be difficult for these molecules/atoms to stick on these surfaces and, therefore, there is a high probability of desorption or diffusion for these molecules/atoms to settle down at sites of higher energy [21]. Since the synthesis of the $GdB_{44}Si_2$ nanostructures was held at a high temperature of 1200 °C, there was a strong tendency for the low-energy surfaces to stay flat and thus drove the subsequently arrived molecules/atoms to diffuse to surfaces of higher energy or stick onto rough edges. As this process continued, the low-energy surfaces would be enlarged to result in a two-dimensional structure as illustrated in Fig. 7b. In Fig. 7c, one can also see that some nanostructures look like nanowires but they actually have belt-like structure at the bottom with unsmooth edges. These nanostructures were formed possibly because the growth process was terminated during the transition from nanowire to nanobelt. Eventually, the side surfaces of higher energy also turned flat and the deposition on them would also stop. The molecules/atoms would continue diffusing along the length to the sites that were still rough and became nanobelts eventually as shown above. Figure 7d is a schematic of the final nanostructure which has also been observed when synthesizing ZnS [20], CdS [24], and $InGeO_7$ [25].

It is also of interest to examine and understand the thermoelectric performance of these nanostructures, and experiments are in progress.

Conclusions

In conclusion, we have successfully synthesized single crystalline $GdB_{44}Si_2$ nanowires and nanobelts using CVD and the structure of these nanostructures have been characterized by high-resolution electron microscopy, electron diffraction, and energy-dispersive X-ray spectroscopy. These nanostructures are of the YB_{50} crystal structure and grew in the [010] direction. The nanowires and nanobelts have thickness of about several tens of nanometers and length of several tens of microns. The nanowire growth follows the VLS mechanism and the nanobelts were formed by a subsequent VS process.

Acknowledgements This work is partially supported by the Development of System and Technology for Advanced Measurement and Analysis, Japan Science and Technology Corporation (JST) and the Nanotechnology Network Project of the Ministry of Education, Culture, Sports, Science, and Technology (MEXT), Japan.

References

1. Bailey JE (1994) Handbook of polymer-fibre composites. Longman Scientific and Technical, Harlow
2. Tavadze FN, Lominadze JV, Khvedelidze AF, Tsagareishvili GV, Shorshorov MK, Bulichev SI (1981) J Less-Common Met 82:95
3. Adams RM (1964) Boron, metallo-boron, compounds and boranes. Interscience Publishers, New York
4. Mori T (2008) Handbook on the physics and chemistry of rare-earths, vol 38. North-Holland, Amsterdam, pp 105–173
5. Mori T (2005) J Appl Phys 97:093703
6. Mori T (2006) Phys B 383:120
7. Tanaka T, Okada S, Ishizawa Y (1994) J Alloys Compd 205:281
8. Mori T (2006) Z Kristallogr 221:464
9. Tanaka T, Okada S, Ishizawa Y (1997) J Solid State Chem 133:55
10. Mori T, Tanaka T (1999) J Alloys Compd 288:32
11. Mori T, Tanaka T (2001) Mat Res Bull 36:2463
12. Higashi I, Kobayashi K, Tanaka T, Ishizawa Y (1997) J Solid State Chem 133:16
13. Mori T, Tanaka T (2001) IEEE Trans Mag 37:2144
14. Mori T, Tanaka T (2003) J Alloys Compd 348:203
15. Zhang H, Zhang Q, Tang J, Qin L-C (2005) J Am Chem Soc 127:2862
16. Zhang H, Zhang Q, Tang J, Qin L-C (2005) J Am Chem Soc 127:8002
17. Zhang H, Zhang Q, Zhao G, Tang J, Zhou O, Qin L-C (2005) J Am Chem Soc 127:13120
18. Wanger RS (1970) Whisker technology. Wiley, New York, pp 47–119
19. Wang ZL (2003) Adv Mater 15:432
20. Moore D, Wang ZL (2006) J Mater Chem 16:3898
21. Dai ZR, Pan ZW, Wang ZL (2003) Adv Funct Mater 13:9
22. Pan ZW, Dai ZR, Wang ZL (2001) Science 291:1947
23. Dai ZR, Pan ZW, Wang ZL (2001) Solid State Commun 118:351
24. Gao T, Wang T (2004) J Phys Chem B 108:20045
25. Yan C, Singh N, Lee PS (2009) Cryst Growth Des 9:3697